The Astronomical Journal, 162:68 (17pp), 2021 August https://doi.org/10.3847/1538-3881/ac052c

Discovery of 22 GHz Water Masers in the Serpens South Region

Gisela N. Ortiz-León[1], Adele L. Plunkett[2], Laurent Loinard[3], Sergio A. Dzib[1], Carolina B. Rodríguez-Garza[4], Thushara Pillai[5], Yan Gong[1], and Andreas Brunthaler[1]
[1] Max Planck Institut für Radioastronomie, Auf dem Hügel 69, D-53121 Bonn, Germany; gortiz@mpifr-bonn.mpg.de
[2] National Radio Astronomy Observatory (NRAO), 520 Edgemont Road, Charlottesville, VA 22903, USA
[3] Instituto de Radioastronomía y Astrofísica (IRyA), Universidad Nacional Autónoma de México Morelia, 58089, Mexico
[4] Tecnologico de Monterrey, Escuela de Ingeniería y Ciencias, Avenida Eugenio Garza Sada 2501, Monterrey, 64849, Mexico
[5] Institute for Astrophysical Research, Boston University, Boston, MA 02215, USA
Received 2021 April 21; revised 2021 May 24; accepted 2021 May 24; published 2021 July 20

Abstract

Using the Karl G. Jansky Very Large Array (VLA), we have conducted a survey for 22 GHz, $6_{1,6}$–$5_{2,3}$ H_2O masers toward the Serpens South region. The masers were also observed with the Very Long Baseline Array following the VLA detections. We detect for the first time H_2O masers in the Serpens South region that are found to be associated to three Class 0–Class I objects, including the two brightest protostars in the Serpens South cluster, known as CARMA-6 and CARMA-7. We also detect H_2O masers associated to a source with no outflow or jet features. We suggest that this source is most probably a background asymptotic giant branch star projected in the direction of Serpens South. The spatial distribution of the emission spots suggest that the masers in the three Class 0–Class I objects emerge very close to the protostars and are likely excited in shocks driven by the interaction between a protostellar jet and the circumstellar material. Based on the comparison of the distributions of bolometric luminosity of sources hosting 22 GHz H_2O masers and 162 young stellar objects covered by our observations, we identify a limit of $L_{\rm Bol} \approx 10 L_{\odot}$ for a source to host water masers. However, the maser emission shows strong variability in both intensity and velocity spread, and therefore masers associated to lower-luminosity sources may have been missed by our observations. We also report 11 new sources with radio continuum emission at 22 GHz.

Unified Astronomy Thesaurus concepts: Water masers (1790); Low mass stars (2050); Star forming regions (1565); Interferometers (805); Protoclusters (1297); Young stellar objects (1834); Protostars (1302)

1. Introduction

Water masers are known to be abundant in low- and high-mass star-forming regions, where they trace collimated outflows (e.g., Furuya et al. 1999, 2000; Hollenbach et al. 2013; Moscadelli et al. 2013) and protoplanetary disks (Fiebig et al. 1996; Torrelles et al. 1998), both of which are key features during the earliest phases of protostellar evolution. In particular, the water maser line from the $J = 6_{1,6}$–$5_{2,3}$ rotational transition at 22 GHz has been detected, since its discovery by Cheung et al. (1969), in hundreds of sources within both high- and low-mass star-forming regions (e.g., Furuya et al. 2003; Moscadelli et al. 2020). These masers are extremely bright and compact, and have become primary targets for Very Long Baseline Interferometry (VLBI), which can probe angular resolutions better than 1 mas (e.g., Wu et al. 2014; Sanna et al. 2017). Observations of 22 GHz water masers have been crucial primarily for the study of the dense gas and their dynamics around young stellar objects (YSOs; Moscadelli et al. 2019).

The earliest phase of low-mass protostellar evolution (the Class 0 phase in the evolutionary classes defined by Lada 1987 and Andre et al. 1993) is characterized by the presence of powerful outflows, which are believed to be intimately linked to the accretion process. These outflows can create shocked regions where the protostellar jets impact the ambient molecular cloud that could collisionally pump H_2O maser emission. Searches for water masers frequently target the youngest low-mass protostars, since they exhibit the most powerful collimated mass outflows. Several systematic surveys to search for water maser emission toward low-mass stars have been conducted in the past (Wilking et al. 1994; Claussen et al. 1996; Furuya et al. 2001, 2003). These surveys have found that the detection rate of water masers drops drastically as protostars evolve through the Class I and II phases (Furuya et al. 2001, 2003). This is explained by the dissipation of the dense gas around the central object as it evolves. Also, the detection rate of water masers does seem to drop significantly for very-low-luminosity objects ($L \lesssim 0.4\, L_{\odot}$; Gómez et al. 2017).

Only a few VLBI studies of the kinematics of water masers in low-mass stars have been conducted in the past (e.g., Claussen et al. 1998; Moscadelli et al. 2006; Imai et al. 2007; Dzib et al. 2018), in part because they are weaker than their counterparts associated to high-mass stars. These studies have shown that the masers emerge at the base of the protostellar jet, in shocks likely driven by the interaction with the disk, or in shocked gas clumps along the axis of the jet (Moscadelli et al. 2006).

In this paper, we focus on the Serpens South region, a well-known region harboring one of nearest very young protostellar clusters. Serpens South was discovered by Gutermuth et al. (2008) from Spitzer images as an infrared dark cloud and since then it has become an interesting target to observe low-mass young stars in the earliest phases of its development. It is located ∼3° south of the Serpens Main cloud, a region also rich in star formation activity (Eiroa et al. 2008). The W40 region, located ∼10′ to the east of Serpens South, is a more evolved star-forming region hosting a cluster of massive stars and an H II region. Serpens South and W40 are both projected within the broader Aquila Rift complex of molecular clouds and often are referred to as the Aquila region (e.g., André et al. 2010).

The distance to the Aquila region has been a matter of debate in the literature. However, recent measurements do seem to converge to ≈440–480 pc (e.g., Ortiz-León et al. 2017; Herczeg et al. 2019; Zucker et al. 2019). Ortiz-León et al. (2017) obtained

Table 1
VLA Observed Epochs

Epoch	Observation Date	VLA Configuration	Continuum			Channel rms (mJy beam^{-1})
			Beam Size ($'' \times ''$)	P.A. ($^\circ$)	rms (μJy beam^{-1})	
1	2019 Jan 19	C	1.08×0.76	-12.5	25	16
2	2019 Jan 26	C	1.27×0.80	-28.7	24	16
3	2019 Feb 2	C	1.16×0.78	-22.8	27	21
4	2019 Feb 8	C $\rightarrow$ B	0.75×0.44	-1.46	21	18

VLBI trigonometric parallaxes of radio continuum sources in Serpens Main and W40 and reported an average distance of 436.0 ± 9.2 pc. Later, Ortiz-León et al. (2018) analyzed Gaia parallaxes of stars in the Aquila region (two stars are projected in the outskirts of Serpens South) and in Serpens Main, delivered as part of the 2nd data release. They found that the Gaia parallaxes from Aquila agree on average with those from Serpens Main and are also consistent with the previous VLBI estimation, although their associated uncertainties are larger. Thus, in the present study we adopt the distance from the VLBI measurement of 436.0 ± 9.2 pc.

Here we use the Karl G. Jansky Very Large Array (VLA) to conduct a survey of water masers toward Serpens South covering the region with the highest density of protostellar objects. Follow-up observations of the VLA-detected water masers were obtained with the Very Long Baseline Array (VLBA). The paper is organized as follows. Section 2 describes the target selection, acquired observations, and data reduction. In Section 3 we present our results and discuss the properties of the detected H_2O emission, the spatial and velocity distribution of maser spots, and the association of the masers with outflow activity. This section also reports the sources detected with radio continuum emission. In Section 4 we discuss the relationship between H_2O maser emission and bolometric source luminosity. Finally, Section 5 presents our conclusions.

2. Observations and Data Reduction

2.1. VLA Observations

We observed the $6_{1,6}$–$5_{2,3}$ H_2O maser line (at rest frequency 22,235.080 MHz) with the *K*-band receiver at a velocity resolution of 0.1 km s^{-1} (corresponding to 7.8 kHz) and a velocity coverage of $\sim$100 km s^{-1}. The observations were taken in four epochs in C and C $\rightarrow$ B[6] configurations (Table 1) under program 18B-230. The epoch observed on 2019 February 2 missed 25% of the scans; therefore, it was reobserved on 2019 February 8 with the C $\rightarrow$ B configuration (Table 1). The water maser line was covered by a 16 MHz wide spectral window with 2048 channels. Eight additional 128 MHz wide spectral windows (with 64 channels each) were observed in each baseband for the continuum, resulting in an aggregate bandwidth of 2 GHz.

A total of 48 VLA fields (Figure 1) were selected to cover essentially all known low-mass protostars across the region. Our target sample includes all Class 0+I candidates[7] reported in Winston et al. (2018; 90 sources) and Dunham et al. (2015; 60 sources), as well as the 67 protostars identified by Plunkett et al. (2018) from ALMA 1 mm continuum observations and infrared (IR) data. The observed area also includes 31 Flat-spectrum, 59 Class II, and 12 Class III objects from the catalog of Dunham et al. (2015).

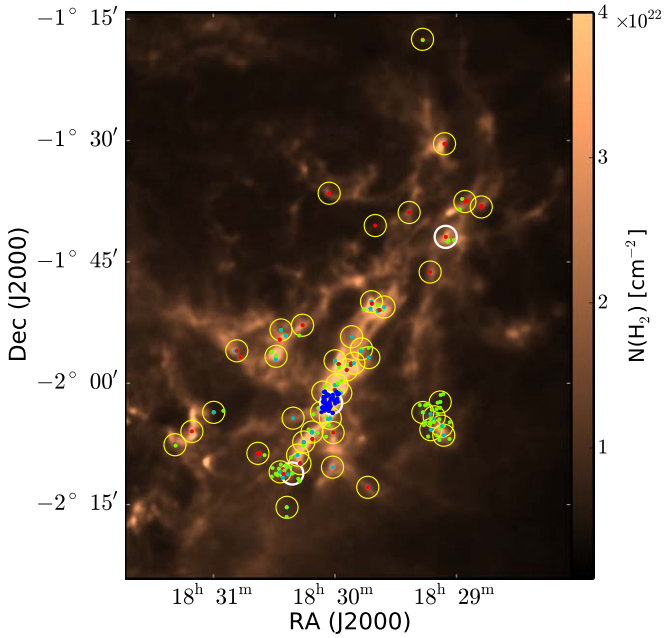

Figure 1. The 48 VLA pointings used for our observations are indicated by the large circles. Fields where H_2O masers are detected are in white. The circle diameters of 2.′7 correspond to the field of view at 22.2 GHz. Cyan dots mark the positions of 90 young stars reported in Winston et al. (2018), which were identified as Class 0+I objects. Red dots correspond to 60 YSO candidates by Dunham et al. (2015) classified as Class 0+I objects. Blue dots are 67 protostars identified by Plunkett et al. (2018) from ALMA 1 mm continuum observations and IR data. The distribution of the VLA pointings was chosen to cover the most of these objects. Green dots correspond to 31 flat-spectrum, 59 Class II, and 12 Class III objects from the catalog of Dunham et al. (2015) that fall within the observed VLA fields. The background is a Herschel H_2 column density map of the Serpens South star-forming region (André et al. 2010).

Observing sessions consisted of series of three scans on target fields (for $\sim$1.8 minutes each target) bracketed by phase-calibrator scans of $\sim$1.4 minutes. The quasar 3C 286 (α(J2000) = 13:31:08.287984, δ(J2000) = +30:30:32.95886), observed at the beginning of the observations, was used as the standard flux and bandpass calibrator, while J1851+0035 (α(J2000) = 18:51:46.7217, δ(J2000) = +00:35:32.414) was used as the phase calibrator. The total observing time in each epoch was about 2.4 hr.

Data calibration was performed with the NRAO's Common Astronomy Software Applications (CASA; version 5.4.1) package using the VLA pipeline[8] provided along with the

[6] C $\rightarrow$ B denotes the reconfiguration from C- to B-array.

[7] Class 0+I refers to objects in the Class 0 or Class I phase, that cannot be separated based on IR measurements alone. Dunham et al. (2015) uses the IR extinction-corrected spectral index, α, with $\alpha \geqslant 0.3$ for Class 0+I. Winston et al. (2018) uses IR colors to identify (deeply) embedded protostars as Class 0+I objects.

[8] https://science.nrao.edu/facilities/vla/data-processing/pipeline/CIPL_54

Table 2
VLBA Observed Epochs

Epoch	Observation Date	Beam Size (mas × mas)	P.A. (°)	Channel rms (mJy beam^{-1})	Observed Targets
A1	2020 Mar 20	1.4 × 0.5	−13	10	CARMA-7, 2MASS J18295902–0201575
A2	2020 Apr 5	1.5 × 0.4	−16	9	CARMA-7, 2MASS J18295902–0201575
A3	2020 Sep 21	1.6 × 0.3	−17	9	CARMA-7
A4	2020 Oct 25	1.3 × 0.4	−17	8	CARMA-6
B1	2020 Mar 27	1.1 × 0.4	−13	10	SSTgbs J1830177–021211, SSTgbs J1829053–014156
B2	2020 Apr 9	1.3 × 0.6	5	10	SSTgbs J1830177–021211, SSTgbs J1829053–014156
B3	2020 Sep 29	1.4 × 0.4	−17	9	SSTgbs J1830177–021211, SSTgbs J1829053–014156
B4	2020 Nov 1	1.4 × 0.4	−17	7	SSTgbs J1830177–021211

data that was modified to work with spectral line observations. The calibrated visibilities were imaged using the CASA task `tclean`. We produced maps of continuum emission for each observed field by integrating the full 2 GHz bandwidth. The pixel size was 0.″16 in the maps from the first three epochs and 0.″073 in the last epoch. The number of clean iterations was set to 10,000 with a threshold for cleaning of 0.066 mJy. We use "Briggs" weighting and applied the primary beam correction. For the image sizes, we used 1040 × 1040 and 2250 × 2250 pixels in C and C → B configuration, respectively, which correspond to a field size of 2.′7. Maps were made for individual epochs and for the combination of the first, second, and fourth epochs. The central frequency (wavelength) in these continuum images is 22.9 GHz (1.31 cm). The beam sizes and root mean square (rms) noise achieved in the continuum images are given in columns 4–6 of Table 1.

For the images of the line data, we first fit and subtract the continuum from the *uv* data using the task `uvcontsub`, excluding the inner 900 channels for the fitting. Then, the task `tclean` was used to generate the data cubes of 2.′7 in size with 1000 clean iterations, a threshold for cleaning of 25 mJy, and the same pixel size and weighting scheme as the continuum images. The average rms noise in the maps not corrected by the primary beam was 16, 16, 21, and 18 mJy beam^{-1} in epochs 1, 2, 3, and 4, respectively (Table 1). In order to obtain the positions and fluxes of the detected spots at individual channels (see Section 3.1), we perform a 2D Gaussian fit to the brightness distribution with the CASA task `imfit`.

The error in the spot position is given by the astrometric uncertainty, $\theta_{\rm res}/(2 \times {\rm S/N})$, where $\theta_{\rm res}$ is the FWHM size of the restoring beam, and S/N the signal-to-noise ratio of the source (Thompson et al. 2017). The C-configuration maps of the H_2O line have an average beam size of 1.″2. Therefore, for emission detected at S/N = 5 the formal (statistical) error in position is ≈0.″12. For the C → B configuration, the statistical error is ≈0.″08.

2.2. VLBA Observations

We conducted multiepoch VLBA observations toward four targets, including the three sources that were undoubtedly detected in H_2O emission with the VLA (Section 3.1), and one more star with tentative detection (2MASS J18295902–0201575). These observations were conducted between 2020 March and November as part of program BO061 (Table 2). The data were taken at 22.2 GHz with four intermediate frequency (IF) bands, each of 16 MHz bandwidth. One IF was centered at the $6_{1,6}$–$5_{2,3}$ H_2O transition and correlated with a channel spacing of ∼0.2 km s^{-1} (15.625 kHz). We observed the quasar J1824+0119 (α(J2000) = 18:24:48.143436, δ(J2000) = +01:19:34.20183) as the phase-reference calibrator, which we alternated with target observations in fast switching mode, switching sources every ≈30 s. Additional 30 minute blocks of calibrators distributed over a wide range of elevations were observed at 23.7 GHz every ≈2 hr during each ≈9 hr observing run. The observations were organized in two blocks, "A" and "B," with each block observing up to two targets. The total on-source time of the water masers was 1.5 and 3 hr for blocks observing two and one targets, respectively (see Table 2). The blocks have been observed in a total of four epochs as of the year 2020 (labeled as 1–4 in Table 2). Here, we only report the detections achieved so far (Section 3.2). The full analysis of the multiepoch VLBA data will be presented in a forthcoming paper.

Data calibration was performed with the Astronomical Imaging System (AIPS; Greisen 2003), using the ParselTongue scripting interface (Kettenis et al. 2006) and following standard procedures for phase-referencing observations (e.g., Reid et al. 2009). Since the VLA-detected masers are relatively weak (<1 Jy; Section 3), the fringe-fitting solutions were derived from the scans on the phase-reference calibrator and then applied to the target. Once the calibration was completed, we imaged individual channel maps of 4096 × 4096 pixels using a pixel size of 50 μas. Spot positions and fluxes were determined by fitting a Gaussian to the brightness distribution at individual channels using the AIPS task `jmfit`. The expected statistical positional errors are of the order of 70 μas for emission detected at S/N = 5.

3. Results

3.1. VLA-detected Sources with H_2O Emission

The cubes of the H_2O line were visually inspected to search for emission at the location of the targets. Only three sources have detected H_2O emission, whose properties are listed in Table 3. Column 1 of this table indicates the name of the source. Column 2 gives the epoch of detection. Column 3 and 4 give the mean position obtained by taking the weighted mean of the contributing maser spots, where "spot" refers to emission detected in a single channel map. Column 5 gives the line-of-sight LSR velocity of the channel with the highest intensity. Column 6 gives the velocity range of H_2O emission. Columns 7 and 8 indicate peak- and integrated-flux density of the highest-intensity channel, respectively. Column 9 gives the water maser luminosity.

In the three detected sources, the H_2O emission is weak, with fluxes below ∼230 mJy and velocity spread $\lesssim$1 km s^{-1}. Figure 2 presents extracted spectra at the position with the highest intensity. From this figure, it is clear that the emission

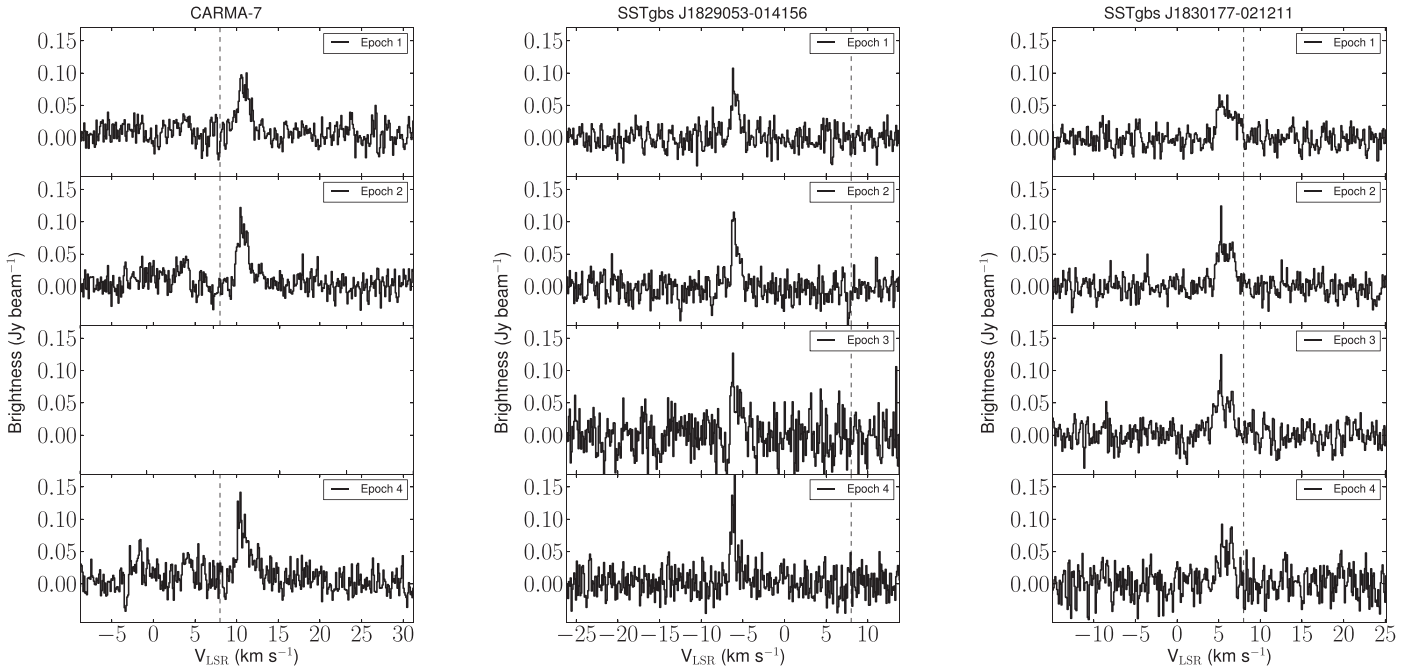

Figure 2. Spectra of H_2O emission detected with the VLA extracted at the peak pixel from the data cubes. The epoch of observation is indicated in the legends. The vertical dashed line at $V_{LSR} = 8$ km s^{-1} marks the systemic velocity of the cloud. Due to failures during the observations, several fields, including CARMA-7, were skipped in the third epoch.

Table 3
Properties of the VLA Detected Sources with 22 GHz Water Emission

Name	Epoch	α (J2000) (h:m:s)	δ (J2000) (°:′:″)	V_{LSR} (km s^{-1})	ΔV_{LSR} (km s^{-1})	Peak Flux (mJy beam^{-1})	Int. Flux (mJy)	L_{H_2O} (10^{-10} $L_\odot$)
(1)	(2)	(3)	(4)	(5)	(6)	(7)	(8)	(9)
CARMA-7[a]	1	18:30:04.12	−02:03:02.56	10.46	1.2	96.70 ± 4.30	92.83 ± 7.70	5.6
	2	18:30:04.12	−02:03:02.56	10.46	1.4	118.27 ± 7.32	115.42 ± 12.76	6.0
	4	18:30:04.12	−02:03:02.49	10.46	0.8	132.19 ± 6.69	172.79 ± 14.34	5.7
SSTgbs J1829053-014156	1	18:29:05.32	−01:41:56.93	−6.18	0.8	104.32 ± 6.46	139.87 ± 14.04	4.1
	2	18:29:05.33	−01:41:56.90	−6.08	0.6	119.33 ± 6.21	89.86 ± 10.17	2.9
	3	18:29:05.34	−01:41:56.96	−6.08	0.2	126.59 ± 7.72	140.77 ± 15.66	1.6
	4	18:29:05.33	−01:41:56.99	−5.97	0.6	166.97 ± 6.58	231.62 ± 14.65	4.7
SSTgbs J1830177-021211	1	18:30:17.72	−02:12:11.59	6.04	0.2	78.26 ± 7.64	66.09 ± 11.95	0.6
	2	18:30:17.72	−02:12:11.64	5.30	0.6	121.87 ± 4.36	118.22 ± 7.55	2.2
	3	18:30:17.72	−02:12:11.70	5.30	0.6	123.83 ± 6.02	126.24 ± 10.61	2.4
	4	18:30:17.71	−02:12:11.72	5.40	0.2	86.99 ± 7.78	71.35 ± 12.95	1.2

Notes. Column 1 is the source name. Column 2 is the observed epoch. Column 3 and 4 give the coordinates of the weighted mean position of all contributing emission spots. Columns 5 and 6 are the velocity of the highest intensity channel and the velocity range of the H_2O emission. Column 7 and 8 give the peak- and integrated-flux density, respectively, at the highest intensity channel and associated errors obtained using `imfit`. Column 9 gives the water maser luminosity.
[a] Due to failures during the observations, CARMA-7 was not observed in the third epoch.

shows variability in both flux and velocity (the velocity range of H_2O emission changes between epochs). This, together with the narrow widths of the lines, which are in the range from 0.7 to 2.5 km s^{-1}, suggest that the detected H_2O emission is presumably due to masers. We also notice that spatially distinct groups of spots contribute to the observed H_2O spectra toward SSTgbs J1829053–014156 and SSTgbs J1830177–021211. These groups of spots may correspond to spatially separated features, where "feature" refers to emission observed in contiguous velocity channels at nearly the same position. Since the poor angular resolution of the VLA does not allow us to unambiguously separate the features, we average all maser spots for the positions reported in Table 3, ignoring the possibility that they may be part of distinct features.

In the following, we discuss each detected source separately.

CARMA-7. Also known as SerpS-MM18a (Maury et al. 2019), it is a Class 0 protostar (Maury et al. 2011) with strong millimeter continuum emission (Plunkett et al. 2015a) and a highly collimated bipolar outflow extending ∼0.16 pc (Plunkett et al. 2015b). Several knots are seen along the outflow, suggesting episodic events that are attributed to variations in the accretion rate of mass onto the protostar. There is a nearby protostar, CARMA-6 (also known as SerpS-MM18b; Maury et al. 2019), located to the southwest of CARMA-7, which also

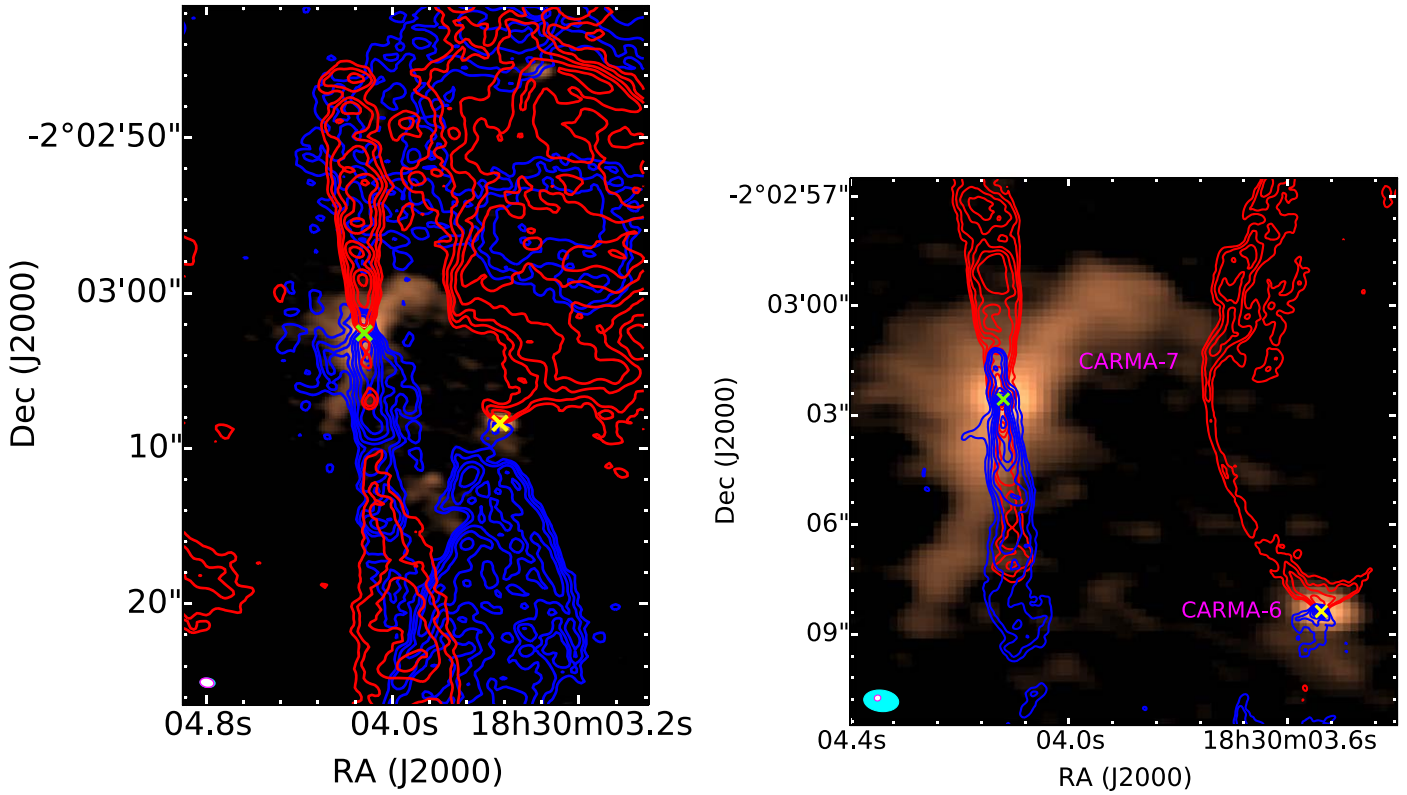

Figure 3. Large-scale molecular outflows traced by CO ($J = 2$–1) at 230.538 GHz from ALMA observations toward CARMA-7 and CARMA-6 (Plunkett et al. 2015b). The integration ranges are −20 to 4 km s^{-1} for the blueshifted component and 12–40 km s^{-1} for the redshifted component. The nth contour is at $(\sqrt{2})^n \times S_{\rm max} \times p$, where $S_{\rm max} = 3.5$ and 6.3 Jy beam^{-1} km s^{-1} (for the blueshifted and redshifted emission, respectively), $n = 0$, 1, 2, 3, 4 ..., and $p = 10\%$. The background is an ALMA map of 1 mm continuum emission (Plunkett et al. 2018). The right panel shows a zoom in of the central part of the mapped region. The contours correspond to CO ($J = 3$–2) emission at 345.796 GHz from ALMA observations, integrated in the same velocity range as the CO ($J = 2$–1) data, with $S_{\rm max} = 10.8$ Jy beam^{-1} km s^{-1}. In both panels, the "X"s indicate the average position of the water masers detected with the VLA (green) and VLBA (yellow; see Section 3.2). The beam sizes are shown in the bottom left corner of the images as white (molecular data) and cyan (continuum emission) ellipses.

has millimeter continuum emission and is classified as a Class 0 +I object (Kern et al. 2016). The molecular outflow associated with CARMA-6 has a much wider opening angle (see Figure 3). The dust masses of CARMA-7 and CARMA-6 are estimated to be 1.21 and 0.43 $M_\odot$, respectively (Plunkett et al. 2015a). They have *internal* luminosities of 13 and 16 $L_\odot$ that were derived from the 70 μm band of Herschel assuming a distance of 350 pc (Podio et al. 2021). These luminosities are rescaled to 20 and 25 $L_\odot$ for a distance of 436 pc.

The water maser detected with the VLA toward CARMA-7 is found at the very base of the CO ($J = 2$–1) molecular outflow (see Figure 3) traced by ALMA (Plunkett et al. 2015b). This position also coincides with the peak of the millimeter continuum emission (see the right panel of Figure 3). The velocity-integrated intensity map of the CO ($J = 3$–2) line is also shown in this figure (right panel). In CARMA-6, the redshifted CO ($J = 3$–2) outflow seems to correspond to the cavity walls of the CO ($J = 2$–1) outflow. Radio continuum sources associated with both CARMA-7 and CARMA-6 were found by Kern et al. (2016) from observations at 4.75–7.25 GHz (their sources VLA 12 and VLA 13). The radio continuum emission is also detected in our observations (see Section 3.3 and Figure 10 in the Appendix; sources #10 and #9). Kern et al. (2016) derived radio spectral indices of 2.31 ± 0.12 and 0.51 ± 0.08 for CARMA-7 and CARMA-6, respectively, which are indicative of thermal radio emission from ionized gas, and proposed that the radio emission is tracing the base of collimated outflows.

SSTgbs J1829053–014156/IRAS 18264-0143. This object is also a known YSO (Dunham et al. 2015). The extinction-corrected slope of the infrared spectral energy distribution (SED) is 0.96, which places the source in the Class 0+I phase (Dunham et al. 2015). The stellar extinction-corrected bolometric luminosity is $L_{\rm Bol} = 2.9\,L_\odot$ obtained by assuming a distance of 260 pc (Dunham et al. 2015). This value is rescaled to 8.2 $L_\odot$ for a distance of 436 pc. There is a 1.2 mm continuum peak close (at $\approx 6''$) to the water maser, called Aqu-MM3, which was identified as a Class 0+I object (Maury et al. 2011). A dust mass of 1.7 $M_\odot$ and a bolometric luminosity of 14.3 $L_\odot$ (corrected for the assumed distance) was measured for the millimeter continuum source. We detected radio continuum emission associated to this source (see Figure 10 in the Appendix; source #2), which may be tracing the base of the jet. The maser position coincides, within the position errors, with the peak of radio continuum (Figure 10 in the Appendix).

We searched the literature for molecular outflows that can be associated with this maser source. Observations of the CO ($J = 3$–2) transition at 345.796 GHz were conducted by Nakamura et al. (2011) with the ASTE 10 m telescope to study the outflow activity in Serpens South. In their images, there is a clear bipolar CO outflow in the vicinity of SSTgbs J1829053–014156 (the redshifted and blueshifted outflow components are called R6 and B11 in the nomenclature of Nakamura et al. 2011). The maser is very close to the base of the blueshifted component (see Figure 9 of Nakamura et al. 2011). This outflow is also traced by H_2 emission at 2.12 μm

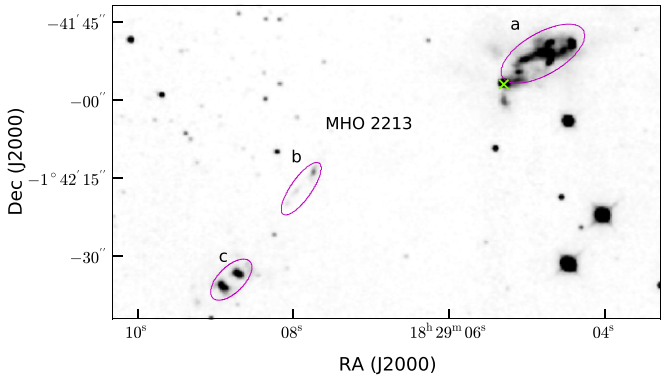

Figure 4. H_2 2.12 μm image of MHO2213, the outflow associated with SSTgbs J1829053–014156/IRAS 18264–0143 (Zhang et al. 2015). The MHO features are marked with magenta ellipses and denoted with letters. The green "X" denotes the position of the maser, which coincides with the position of the outflow driving source.

(Davis et al. 2010; Zhang et al. 2015). The associated molecular hydrogen emission-line object is MHO 2213, which is thought to be driven by IRAS 18264–0143. The position angle of 118° of the MHO is similar to the orientation of the CO outflow (see Figure 4). The maser is located at the base of the MHO feature that is associated with the blueshifted CO lobe.

SSTgbs J1830177–021211/IRAS 18276–0214. This object is a known YSO (Dunham et al. 2015; Winston et al. 2018). The infrared SED has a extinction-corrected slope of −2.22 (Dunham et al. 2015), which places it in the Class III phase. Later, based on its infrared colors, Winston et al. (2018) classified it as a disk-bearing pre-main-sequence object (equivalent to the Class II/transition disk class of Dunham et al. 2015). The extinction-corrected bolometric luminosity is $L_{\rm Bol} = 158\,L_{\odot}$, which has been rescaled for a distance of 436 pc. Its mass has not been estimated.

The detection of water maser emission in this source is unexpected given that earlier surveys have suggested that maser activity disappears after the main accretion and outflow (Class 0–Class I) phase (Furuya et al. 2001). The maser has also been detected in our follow-up VLBA observations (see Section 3.2). We did not detect radio continuum emission associated to the maser and no radio continuum has been reported in the literature either. There are three molecular outflow lobes (B14, B15, and R8 in the nomenclature of Nakamura et al. 2011) in the surroundings of the water maser as seen in Figure 5, where we show CO (J = 1–0) data at 115.27 GHz taken with the Nobeyama telescope (Nakamura et al. 2019). The outflow lobes identified by Nakamura et al. (2011) are indicated in this figure, as well as the positions of the putative driving sources, which are taken from the Herschel catalog of protostellar cores (Könyves et al. 2015). The CO (J = 1–0) emission at the position of the maser is relatively weak. The H_2 2.12 μm image is dominated by very strong emission from IRAS 18276–0214 (Figure 12.9 in Zhang et al. 2015), so it is difficult to find an association with an H_2 outflow feature.

3.2. VLBA Detected Sources with H_2O Maser Emission

SSTgbs J1830177–021211/IRAS 18276–0214. The maser emission is seen at $V_{\rm LSR}$ from 4.2–6.6 km s^{-1} (left panel in Figure 6). These velocities are blueshifted with respect to the velocity of the cloud of 8 km s^{-1} (Kirk et al. 2013) by a few

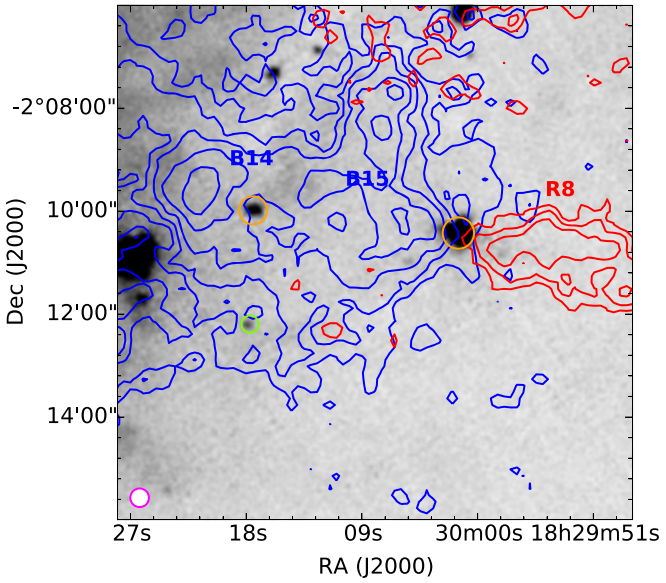

Figure 5. Molecular outflow lobes traced by CO (J = 1–0) at 115.27 GHz (Nakamura et al. 2019) toward SSTgbs J1830177–021211. The integration ranges are −15 to 4 km s^{-1} for the blueshifted component and 11–30 km s^{-1} for the redshifted component. The labels denote lobes identified by Nakamura et al. (2011) from CO (J = 3–2) observations at 345.796 GHz. The nth contour is at $(\sqrt{2})^n \times S_{\rm max} \times p$, where $S_{\rm max} = 0.2$ K km s^{-1}, $n = 0, 1, 2, 3, 4$ ..., and $p = 11\%$. In the background we show a Herschel 70 μm map retrieved from the Science Archive (http://archives.esac.esa.int/hsa/whsa/). Orange circles mark the location of the Herschel protostellar cores (Könyves et al. 2015) that have been identified as the outflow driving sources (Nakamura et al. 2019). The source with detected H_2O masers is indicated by the green circle. The beam size is shown in white in the bottom left corner.

km s^{-1}. The brightest spot has a peak flux of 0.2 Jy beam^{-1}, which is higher than the highest flux detected with the VLA. Figure 7 shows the spatial distribution of the VLBA detected maser spots in four epochs. We identify four main features that occupy an extent of about 2 mas (≈0.9 au) and are aligned roughly along the northeast-southwest direction. The strongest feature, labeled #1, has persisted over the four observed epochs, which cover a time baseline of ≈7 months. Features #2 and #3 were detected on the first and second epochs, and feature #4 only on the second epoch. Table 4 gives the error-weighted mean position offsets and intensity-weighted $V_{\rm LSR}$ for each feature obtained from all contributing spots to that feature. These positional offsets are with respect to the position of feature #1, which we fixed at the origin in all epochs. Figure 7 shows that feature #2 (panel (d)) moved toward the southeast, while feature #3 (panel (c)) moved toward the east between two consecutive epochs separated by only 13 days. Since feature positions are relative to feature #1, we can investigate the internal proper motions of the two features, #2 and #3. In doing this, we remove the effect of the parallax, which is not well constrained by the current data. We obtain proper motions of $(\mu_\alpha \cos\delta, \mu_\delta) = (1.9 \pm 0.8, -2.6 \pm 1.2)$ mas yr^{-1} for feature #2 and $(\mu_\alpha \cos\delta, \mu_\delta) = (-4.7 \pm 3.0, 3.7 \pm 1.0)$ mas yr^{-1} for feature #3. Although small, and given the fact that the positional offsets are larger than the astrometric uncertainties of about 70 μas (Section 2.2), these motions suggest that the two features are moving toward each other. We attempt to estimate the *absolute* proper motions of feature #1 by fitting the positions of the spot detected at $V_{\rm LSR} = 6.1$ km s^{-1}, where the proper motions are free parameters and the parallax is fixed to a constant value. We found that the resulting

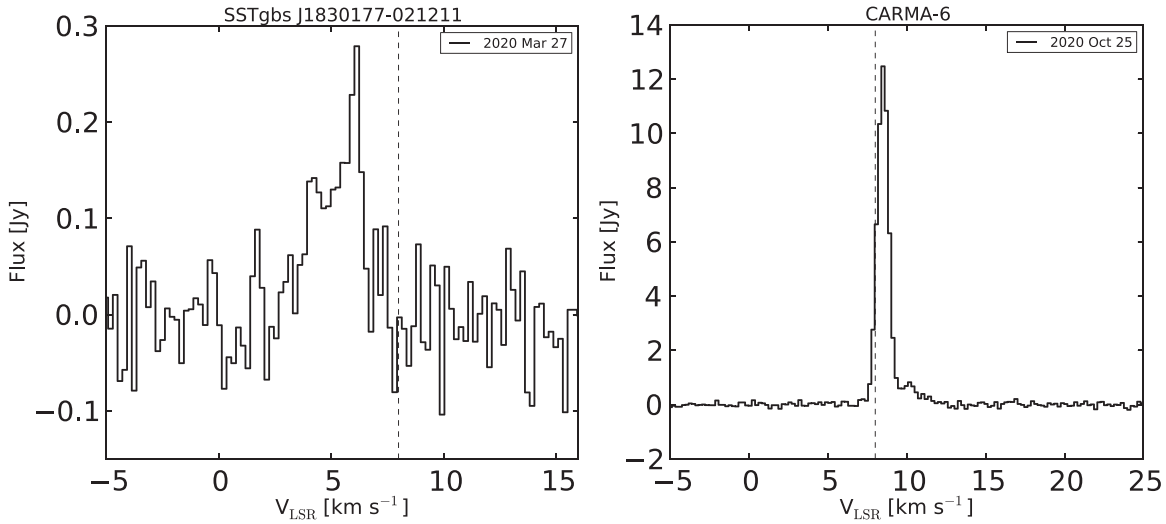

Figure 6. VLBA spectra of the 22 GHz H_2O maser transition toward SSTgbs J1830177–021211/IRAS 18276–0214 (left) and CARMA–6 (right) obtained by integrating over an area that covers all detected spots. The legends indicate the epoch of the observation. The vertical dashed line at $V_{LSR} = 8$ km s^{-1} marks the systemic velocity of the cloud.

Table 4
Properties of the Maser Features Detected with the VLBA

Source	α(J2000)[a]	δ(J2000)[a]	Feature	Epoch	R.A. Offset	Decl. Offset	V_{LSR}[b]	L_{H_2O}
	(h:m:s)	(°:′:″)	#		(mas)	(mas)	(km s^{-1})	(10^{-10} $L_\odot$)
(1)	(2)	(3)	(4)	(5)	(6)	(7)	(8)	(9)
SSTgbs J1830177–021211	18:30:17.7141494	−02:12:11.685739	1	B1	-0.00 ± 0.00	0.00 ± 0.06	6.2	46
			2	B1	0.72 ± 0.02	0.98 ± 0.04	4.6	
			3	B1	1.48 ± 0.04	0.68 ± 0.09	5.3	
	18:30:17.7141433	−02:12:11.685734	1	B2	0.00 ± 0.04	0.00 ± 0.03	6.2	218
			2	B2	0.79 ± 0.01	0.89 ± 0.01	4.6	
			3	B2	1.31 ± 0.11	0.81 ± 0.04	5.5	
			4	B2	1.75 ± 0.07	1.07 ± 0.03	6.6	
	18:30:17.7142092	−02:12:11.685789	1	B3	0.00 ± 0.05	0.00 ± 0.06	6.2	5
	18:30:17.7142152	−02:12:11.686065	1	B4	0.00 ± 0.05	0.00 ± 0.04	6.3	17
CARMA–6	18:30:03.5380	−02:03:08.377	1	A4	-3.47 ± 0.06	2.85 ± 0.06	11.3	1.2
			2	A4	-2.81 ± 0.05	2.43 ± 0.07	10.2	
			3	A4	-0.94 ± 0.01	0.06 ± 0.15	9.4	
			4	A4	-0.00 ± 0.01	0.01 ± 0.18	8.5	

Notes.
[a] Reference position at the given epoch.
[b] Line-of-sight velocity of the feature obtained as the intensity-weighted mean V_{LSR} of the contributing spots.

proper motions largely depend on the assumed value for the parallax. In addition, the fits yield lower residuals for parallaxes that are in the range from 0.5–1.0 mas. Further observations spanning a larger time baseline will allow us to determine if the relative motions we measured continue over time and disentangle *absolute* proper motions from the parallax.

In Figure 5, we see weak blueshifted CO emission around the location of the masers that supports the presence of a molecular outflow that is too weak to be detected. This could happen if the star is not in Serpens South, but behind the molecular cloud, which could absorb the emission from the outflow. We searched the Gaia Early Data Release 3 catalog and found astrometric solution for the optical counterpart of SSTgbs J1830177–021211. The parallax reported in this catalog is 1.52 ± 0.84 mas (Gaia Collaboration et al. 2016, 2021), which is still consistent (within the errors) with a distance of 436 pc, although it may suggest a larger distance. Additional observations of the maser spots will allow us to also fit the parallax and provide an independent measurement of the distance to the star.

It is important to note that the classification of SSTgbs J1830177–021211 as a YSO is based on the infrared spectral index (Dunham et al. 2015). However, asymptotic giant branch (AGB) stars with infrared excesses can be misidentified as YSOs and the contamination fraction is nonnegligible among Class II–Class III sources (Oliveira et al. 2009). Thus, SSTgbs J1830177–021211 could be a background AGB star with the water masers probably tracing an expanding or contracting circumstellar envelope. Given the small relative proper motions we measured for two maser features and the fact that smaller parallaxes are favored from the astrometric fits and are within

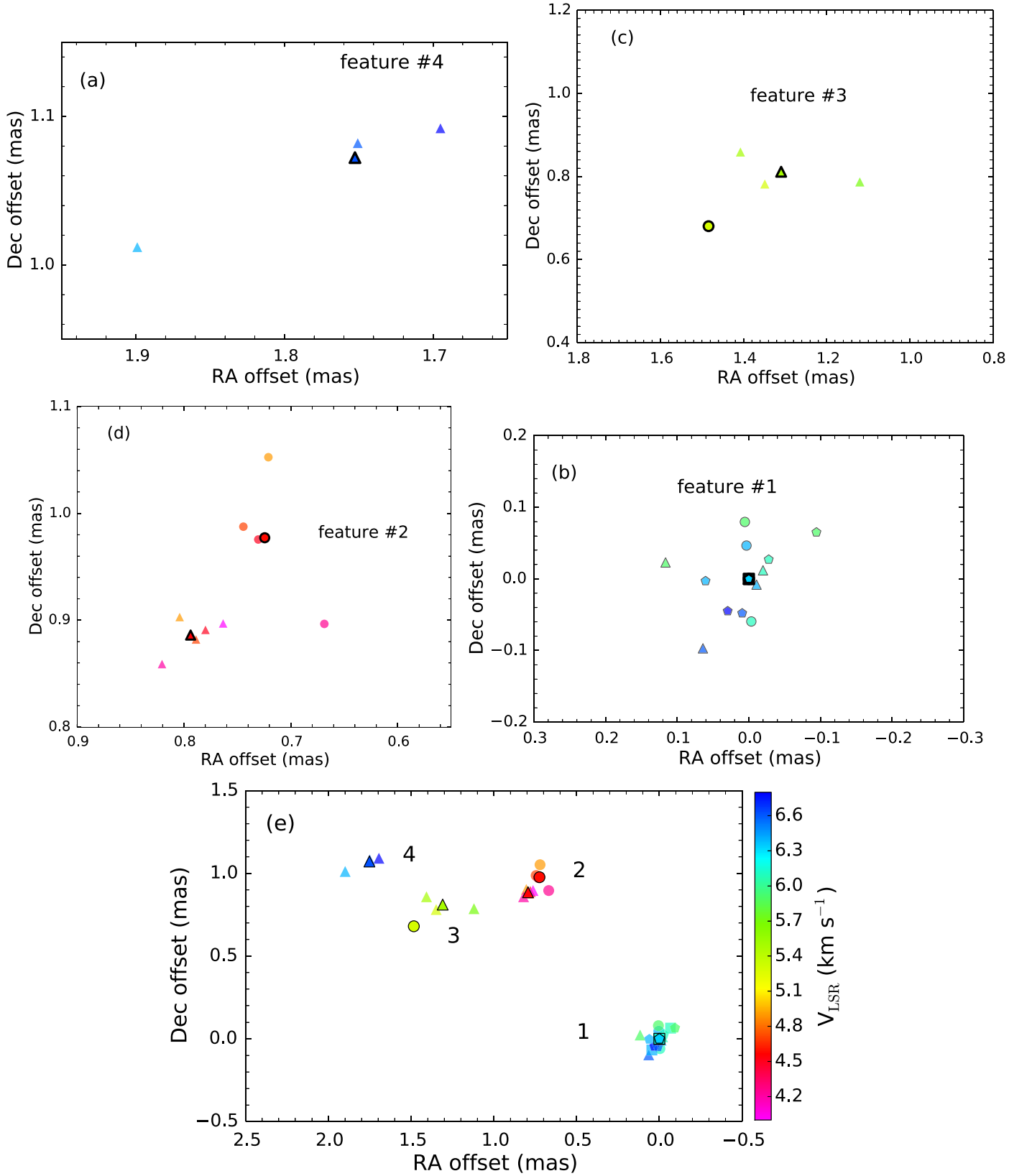

Figure 7. Spatial distribution of the maser spots detected with the VLBA toward SSTgbs J1830177–021211. The position offsets are with respect to the error-weighted mean position of feature #1. The spots are color coded by the LSR velocity (color bar). We use different symbols to distinguish between four epochs observed during 2020 as follows: circles—March 27, triangles—April 9, squares—September 29, and pentagons—November 1. For each epoch and feature, the symbol with black edge indicates the error-weighted mean position of all contributing spots. Panels (a)–(d) show close-up views of the features plotted in panel (e).

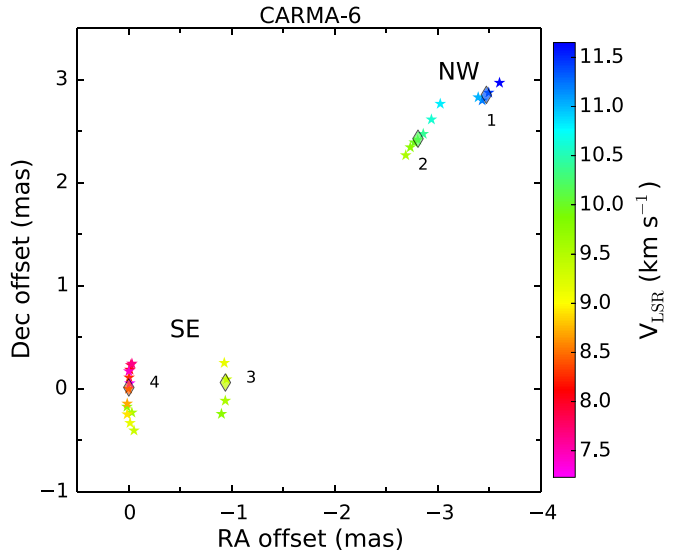

Figure 8. Spatial distribution of the maser spots detected with the VLBA toward CARMA-6. The spots are color coded by the LSR velocity (color bar). The stars indicate offsets measured on 2020 October 25, which are relative to α(J2000) = 18:30:03.538, δ(J2000) = −02:03:08.377. For each feature, the diamonds indicate the error-weighted mean position of all contributing spots to that feature.

the 1σ uncertainty of the Gaia-based parallax measurement, we incline toward the AGB star scenario as the most plausible interpretation.

CARMA-6. Although we did not detect the maser associated with CARMA-7 using the VLBA, we did find a very bright maser (∼12 Jy beam^{-1}) associated with CARMA-6. This maser was seen serendipitously in our VLBA data on 2020 September, albeit it was not detected previously with the VLA in all three observed epochs. Considering the rms noise level of the VLA observations (see Table 1), the VLBA detection of CARMA-6 implies an increase of maser flux density by more than two orders of magnitude in the highest intensity channel. This may correspond to a flare event, although less prominent than water maser flares seen toward massive stars (e.g., Hirota et al. 2014; Volvach et al. 2019). Additional data correlation at the position of CARMA-6 was obtained in a subsequent epoch. The spectrum observed in 2020 October is shown in Figure 6, after integrating over the area containing all maser spots. Figure 8 shows the spatial and velocity distribution of the spots detected in the images. Because the maser is very bright, in this case we phase referenced the visibility data to the maser spot at $V_{LSR} = 8.5$ km s^{-1}.

We detect four groups of spots or *features* that are oriented in the southeast-northwest direction, covering an angular extent of about 4 mas (1.7 au). The groups located to the northwest (NW), hereafter the NW cluster, delineate a nearly straight filament. The emission is redshifted with respect to the systemic velocity of the cloud (8 km s^{-1}), covering LSR velocities smaller than the redshifted lobe of the CO ($J = 2$–1) outflow traced by ALMA at larger angular scales (Figure 3). We see a velocity gradient through the filament with LSR velocities increasing to the north. The groups seen to the southeast (SE), hereafter the SE cluster, show LSR velocities close to the systemic velocity. Here, the maser spots are distributed along two opposite arc-like structures, displaying velocity gradients through the arcs, with LSR velocities increasing to the south. Similar gradients have been seen for instance in Serpens SMM1 (Moscadelli et al. 2006; their Figure 3). In Figure 8, the diamonds indicate the error-weighted mean position of all contributing emission spots (indicated by the stars) to each particular feature. The line-of-sight velocity of each feature is obtained as the intensity-weighted mean V_{LSR} of the contributing spots. Figure 8 shows that the line-of-sight velocities of the features increase to the north. We argue that the water masers originate in shocks between the red lobe of the molecular outflow and the surrounding material. As mentioned above, the NW and SE clusters draw a linear structure with the velocity gradient through this structure. The velocity gradient may arise from a rotating protostellar jet. Observationally, rotation signatures in jets have been seen as velocity gradients perpendicular to the jet axis (e.g., Chen et al. 2016; Lee et al. 2017). In CARMA-6, the orientation of the protostellar jet axis is not yet very well constrained. In the left panel of Figure 3 we see that the molecular outflow is oriented close to the north–south direction, thus the jet may be oriented in the same direction. This seems to be supported by the orientation of the dust disk detected in the ALMA continuum map at 347 GHz shown in Figure 13 in the Appendix. The deconvolved size of this disk is $0\farcs2 \times 0\farcs14$ with a position angle of 82°. If the jet is perpendicular to the disk, the jet position angle would be 172°; while the water maser filament has a position angle of ≈130°. This seems to work against a rotating protostellar jet as the explanation for the observed maser velocity gradient.

In Figure 13 in the Appendix we compare the positions of the maser spots (phase referenced to the extragalactic calibrator) against the distribution of the ALMA continuum emission at 347 GHz. We see that the spots are located within the disk, but have a significant offset of 50 mas (≈22 au) with respect to the continuum peak; the astrometric accuracy of the ALMA observations is about 9 mas.[9] Because the water masers appear to locate at the base of the outflow (and within the protostellar disk) and the linear scale of the masers of 1.7 au is smaller than the typical size of protostellar disks (≲60 au; Maury et al. 2019), the velocity gradient may inherit the velocity structure of the disk. Therefore, the observed water maser flare and the velocity gradient may be directly linked to a disk episodic accretion burst in CARMA-6.

The two epochs where the masers were detected are separated by only two months, covering a time baseline too short to investigate the internal kinematics of the masers. Additional VLBA observations will allow us to establish the kinematic structure of the water masers and further investigate the above alternative scenarios.

3.3. Continuum Sources Detected with the VLA

We performed a visual inspection of the maps that were constructed for the 48 VLA fields, first looking at the individual epochs and then at the maps of the combination of the data from three epochs (see Section 2.1). The visual inspection was done in the images uncorrected for the primary beam response, as this correction increases the noise toward the field edges affecting weak sources that then may appear as noise. However, once identified, the properties of the sources are measured in the primary beam corrected images. Maps of $9'' \times 9''$ in size around the location of detected sources are presented in Figures 10–12 in the Appendix. The maps are for all available epochs, but we note that some epochs do not exhibit detection. Table 5 lists the 17 sources detected with radio continuum, as well as their positions and fluxes as obtained by fitting the brightness distribution with a Gaussian

[9] https://help.almascience.org/kb/articles/what-is-the-astrometric-accuracy-of-alma

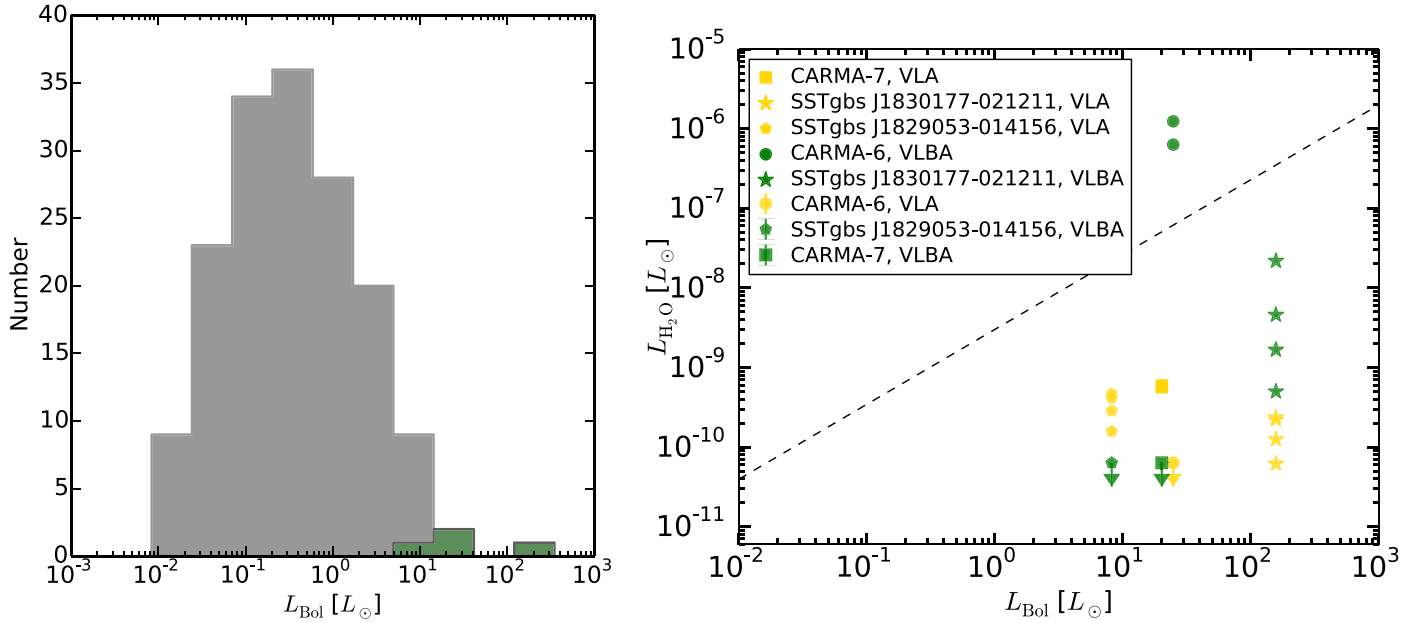

Figure 9. Left: bolometric luminosity distribution of 162 YSOs covered by our VLA observations in gray and the 4 objects with detected water maser emission. Right: water maser luminosity vs. bolometric luminosity for the objects detected with the VLA and the VLBA as described in the legend. The arrows indicate upper limits. The dashed line represents the empirical relation expressed by Equation (3) (Shirley et al. 2007).

model using the task `imfit` in CASA. The fluxes are listed for each epoch and for the combined image.

Not all detected sources with radio continuum are associated with known young stars or other type of objects; there are five sources that have no counterparts (within a radius of 2″) in SIMBAD.[10] On the other hand, we found that 10 sources are associated with known or candidate YSOs (Povich et al. 2013), and another two are associated with known radio sources (Condon et al. 1998; Ortiz-León et al. 2015; Kern et al. 2016), also within a radius of 2″. Table 5 gives the names of the known sources. Out of the 12 objects that have an association with a known source, six had not been detected before in the radio according to SIMBAD. Therefore, we are reporting $6+5=11$ new radio continuum detections.

The newly detected radio continuum sources with no counterparts at any other wavelength are #1, #5, #14, #15, and #17. Source #1 is detected in the four observed epochs with fluxes of 1.7–1.9 mJy. The other sources (#5, #14, #15, and #17) are detected in only one epoch, with fluxes above 0.22 mJy. In addition, sources #3 and #12, which have been reported before in the literature, do not have counterparts at any other wavelength as well.

Following Anglada et al. (1998), we can estimate the number of expected background sources inside a field of diameter θ_F as,

$$N = 1.4\left\{1-\exp\left[-0.0066\left(\frac{\theta_F}{\rm arcmin}\right)^2\left(\frac{\nu}{\rm 5GHz}\right)^2\right]\right\} \times\left(\frac{S_0}{\rm mJy}\right)^{-0.75}\left(\frac{\nu}{\rm 5GHz}\right)^{-2.52}, \quad (1)$$

where S_0 is the detectable flux density threshold and ν the observing frequency. In our observations, $\nu=22.2$ GHz and $S_0=3\times{\rm rms}\approx0.09$ mJy (see Section 2.1). Using a field size of $\theta_F=2\farcm7$, we obtain ≈7 expected background objects in the 48 observed fields. Thus, all of the unclassified sources with detected radio continuum emission are probably extragalactic objects.

Since our targets were observed in multiple epochs, covering a timescale of about three weeks, we can investigate the variability of continuum emission between the epochs. We estimated the variability as the difference between the maximum and minimum peak flux density, normalized by the maximum flux. For the estimation of variability uncertainties, we adopted a flux density calibration error of 15%,[11] which was added quadratically to the statistical errors obtained from the Gaussian fits. We found that nine sources show high levels of variability, with variations $\gtrsim$50% at 3σ. These sources are #4, #5, #11, #12, #13, #14, #15, #16, and #17. Four of these objects are YSOs; the other five are background candidates. Thus, in terms of variability, we do not see a distinction between the two groups. Previous works have found a similar result at shorter radio wavelengths. For instance, Kounkel et al. (2017) showed that both YSOs and extragalactic objects show strong radio continuum variability at 7.5 GHz.

4. Discussion

The four sources with H_2O maser emission detected here are known to be associated with phenomena related to YSOs. However, while CARMA-7, CARMA-6, and SSTgbs J1829053–014156are in the early Class 0–Class I phase, SSTgbs J1830177–021211 is probably in the more evolved Class II phase. Three of the sources with associated maser emission drive large-scale outflows. From the spatial distribution of the maser spots, we argue that in all these sources the masers originate very close to the star and are excited by the

[10] http://simbad.u-strasbg.fr/simbad/

[11] https://science.nrao.edu/facilities/vla/docs/manuals/oss/performance/fdscale

Table 5
Properties of the VLA Detected Radio Continuum Sources

Source ID (1)	Epoch (2)	α (J2000) (h:m:s) (3)	δ (J2000) (°:′:″) (4)	Peak Flux (mJy beam^{-1}) (5)	Int. Flux (mJy) (6)	Known Name (7)	Object[a] Type (8)	References[a] (9)	New[b] Detection? (10)
1	1	18:29:04.88	−01:30:06.2	1.75 ± 0.02	1.78 ± 0.03				Y
1	2	18:29:04.88	−01:30:06.1	1.63 ± 0.02	1.67 ± 0.04				
1	3	18:29:04.89	−01:30:06.1	1.91 ± 0.04	1.84 ± 0.07				
1	4	18:29:04.88	−01:30:06.2	1.89 ± 0.05	1.93 ± 0.10				
1	all	18:29:04.88	−01:30:06.2	1.85 ± 0.02	1.89 ± 0.04				
2	1	18:29:05.33	−01:41:57.0	0.75 ± 0.02	0.79 ± 0.03	IRAS 18264-0143	Y*O	1	Y, H_2O
2	2	18:29:05.33	−01:41:57.0	0.73 ± 0.02	0.78 ± 0.03				
2	3	18:29:05.32	−01:41:56.9	0.72 ± 0.04	0.79 ± 0.07				
2	4	18:29:05.33	−01:41:57.0	0.71 ± 0.02	0.78 ± 0.04				
2	all	18:29:05.33	−01:41:57.0	0.80 ± 0.01	0.91 ± 0.03				
3	1	18:29:06.29	−02:07:48.1	6.94 ± 0.29	6.78 ± 0.51	PMN J1829-0207	Rad	2	
3	2	18:29:06.29	−02:07:48.1	8.45 ± 0.34	9.89 ± 0.67				
3	3	18:29:06.29	−02:07:48.2	8.51 ± 0.28	9.05 ± 0.52				
3	4	18:29:06.29	−02:07:48.1	7.07 ± 0.09	7.34 ± 0.17				
3	all	18:29:06.29	−02:07:48.1	8.03 ± 0.15	8.34 ± 0.28				
4	1	⋯	⋯	<0.34	⋯	2MASS J18291560-0204503	Y*O	3	Y
4	2	18:29:15.62	−02:04:50.3	2.75 ± 0.06	2.82 ± 0.10				
4	4	⋯	⋯	<0.18	⋯				
4	all	18:29:15.62	−02:04:50.3	1.15 ± 0.04	1.42 ± 0.08				
5	1	18:29:51.04	−01:54:24.4	0.22 ± 0.01	0.18 ± 0.02				Y
5	2	⋯	⋯	<0.06	⋯				
5	4	⋯	⋯	<0.06	⋯				
5	all	⋯	⋯	<0.06	⋯				
6	1	18:30:01.36	−02:10:25.7	0.32 ± 0.01	0.33 ± 0.03	2MASS J18300136-0210256, G028.5480+03.7663	Y*O	1	Y
6	2	18:30:01.36	−02:10:25.7	0.37 ± 0.01	0.36 ± 0.03				
6	4	18:30:01.36	−02:10:25.7	0.32 ± 0.01	0.31 ± 0.02				
6	all	18:30:01.35	−02:10:25.7	0.38 ± 0.01	0.38 ± 0.02				
7	1	18:30:03.12	−01:36:32.9	0.16 ± 0.02	0.16 ± 0.03	G029.0540+04.0193	Y*?	4	Y
7	2	18:30:03.12	−01:36:33.1	0.15 ± 0.01	0.18 ± 0.03				
7	3	⋯	⋯	<0.10	⋯				
7	4	⋯	⋯	<0.09	⋯				
7	all	18:30:03.12	−01:36:32.9	0.19 ± 0.01	0.20 ± 0.01				
8	1	⋯	⋯	<0.10	⋯	MHO 3247, G028.6658+03.8174, [KKT2016] VLA 11	Y*O, Rad	5	
8	2	18:30:03.38	−02:02:45.8	0.15 ± 0.01	0.13 ± 0.02				
8	4	⋯	⋯	<0.08	⋯				
8	all	18:30:03.37	−02:02:45.8	0.19 ± 0.02	0.23 ± 0.03				
9	1	18:30:03.54	−02:03:08.4	0.63 ± 0.03	0.55 ± 0.05	SSTYSV J183003.48-020308.5, CARMA-6, [KKT2016] VLA 13	Y*O, Rad	3	H_2O
9	2	18:30:03.54	−02:03:08.3	0.73 ± 0.02	0.71 ± 0.04				
9	4	18:30:03.54	−02:03:08.4	0.56 ± 0.02	0.54 ± 0.03				
9	all	18:30:03.54	−02:03:08.4	0.77 ± 0.02	0.72 ± 0.04				
10	1	18:30:04.11	−02:03:02.5	0.29 ± 0.01	0.44 ± 0.03	CARMA-7, [KKT2016] VLA 12	Y*O, Rad	1	H_2O
10	2	18:30:04.12	−02:03:02.7	0.35 ± 0.02	0.40 ± 0.03				
10	4	18:30:04.13	−02:03:02.6	0.28 ± 0.01	0.37 ± 0.03				
10	all	18:30:04.12	−02:03:02.6	0.38 ± 0.02	0.51 ± 0.04				
11	1	⋯	⋯	<0.09	⋯	2MASS J18300580-0201444, [KKT2016] VLA 7	Y*O, Rad	5	
11	2	⋯	⋯	<0.11	⋯				
11	3	18:30:05.82	−02:01:44.6	0.23 ± 0.01	0.21 ± 0.02				
11	4	⋯	⋯	<0.11	⋯				
11	all	18:30:05.82	−02:01:44.4	0.21 ± 0.01	0.28 ± 0.03				
12	1	18:30:09.69	−02:00:32.7	0.61 ± 0.03	0.50 ± 0.05	GBS-VLA J183009.68-020032.7	Rad	6	
12	2	⋯	⋯	<0.21	⋯				

Table 5
(Continued)

Source ID (1)	Epoch (2)	α (J2000) (h:m:s) (3)	δ (J2000) (°:′:″) (4)	Peak Flux (mJy beam^{-1}) (5)	Int. Flux (mJy) (6)	Known Name (7)	Object[a] Type (8)	References[a] (9)	New[b] Detection? (10)
12	3	⋯	⋯	<0.27	⋯				
12	4	⋯	⋯	<0.21	⋯				
12	all	18:30:09.68	−02:00:32.7	0.48 ± 0.03	0.53 ± 0.05				
13	1	18:30:25.88	−02:10:43.0	0.25 ± 0.01	0.29 ± 0.02	2MASS J18302593-0210420, G028.5908+03.6734	Y*O	1	Y
13	2	18:30:25.88	−02:10:42.8	0.39 ± 0.03	0.34 ± 0.06				
13	3	⋯	⋯	<0.12	⋯				
13	4	18:30:25.88	−02:10:42.9	0.31 ± 0.01	0.31 ± 0.02				
13	all	18:30:25.88	−02:10:42.9	0.36 ± 0.02	0.40 ± 0.03				
14	1	⋯	⋯	<0.11	⋯				Y
14	2	⋯	⋯	<0.09	⋯				
14	3	⋯	⋯	<0.17	⋯				
14	4	18:30:28.63	−01:53:32.6	0.23 ± 0.01	0.21 ± 0.02				
14	all	18:30:28.63	−01:53:32.7	0.19 ± 0.01	0.16 ± 0.02				
15	1	18:30:34.12	−01:56:37.5	0.60 ± 0.04	0.67 ± 0.09				Y
15	2	⋯	⋯	<0.33	⋯				
15	4	⋯	⋯	<0.19	⋯				
15	all	18:30:34.12	−01:56:37.6	0.65 ± 0.03	0.62 ± 0.05				
16	1	⋯	⋯	<0.06	⋯	IRAS 18280-0210, G028.6435 +03.6457	Y*O	3	Y
16	2	⋯	⋯	<0.12	⋯				
16	3	18:30:37.61	−02:08:40.1	0.23 ± 0.02	0.29 ± 0.03				
16	4	⋯	⋯	<0.12	⋯				
16	all	18:30:37.61	−02:08:40.2	0.19 ± 0.01	0.21 ± 0.02				
17	1	⋯	⋯	<0.10	⋯				Y
17	2	⋯	⋯	<0.08	⋯				
17	3	⋯	⋯	<0.13	⋯				
17	4	18:31:13.29	−02:05:46.2	0.65 ± 0.02	0.63 ± 0.03				
17	all	18:31:13.29	−02:05:46.2	0.22 ± 0.01	0.17 ± 0.02				

Notes.
[a] Classification taken from the literature: young stellar object (Y*O), young stellar object candidate (Y*?), and known radio source (Rad). References: (1) Maury et al. (2011); (2) Condon et al. (1998) (3); Winston et al. (2018); (4) Povich et al. (2013); (5) Plunkett et al. (2018); (6) Ortiz-León et al. (2015).
[b] This flag indicates whether the source is a new radio continuum detection (Y) and/or has detected maser emission (H_2O).

interaction between molecular outflows with the surrounding dense material, likely of the circumstellar disk.

Extinction-corrected bolometric luminosities are available for the 162 stars of the catalog by Dunham et al. (2015) that were observed with the VLA. The distribution of the bolometric luminosities, which have been rescaled assuming a distance of 436 pc, are shown in the left panel of Figure 9. Also shown in this figure are the bolometric luminosities of SSTgbs J1829053–014156 and SSTgbs J1830177–021211, and the internal luminosities of CARMA-7 and CARMA-6. As expected, maser emission was detected toward the objects with the highest luminosity. Figure 9 suggests that there is a bolometric luminosity threshold of $L_{\rm Bol} \approx 10\,L_{\odot}$ to excite water maser emission. However, water masers have been detected in objects with lower luminosities before (Furuya et al. 2003); for example, in VLA 1623 ($L_{\rm Bol} \approx 1\,L_{\odot}$, $d = 138$ pc; Andre et al. 1993; Ortiz-León et al. 2018) and GF 9-2 ($L_{\rm Bol} \approx 0.3$–$1.7\,L_{\odot}$, $d = 200$–474 pc; Furuya et al. 2008; Podio et al. 2021). It is still possible that the detection of water masers associated to lower-luminosity objects in Serpens South was missed due to variability. For instance, in CARMA-6, the masers were not detected in the three observed epochs with the VLA, but serendipitously detected with the VLBA about 1.5 years later.

We estimate water maser luminosities according to

$$L_{\rm H_2O} = 4\pi d^2 S_{\rm int} \Delta V \nu_0 / c, \quad (2)$$

where $S_{\rm int}$ is the maser integrated-flux density, ΔV is the velocity range of maser emission, $\nu_0 = 22{,}235.080$ MHz is the rest frequency of the $J = 6_{1,6}$–$5_{2,3}$ water line, c the speed of light, and d the distance to the source. The water mater luminosities are listed in Column 9 of Tables 3 and 4 for sources detected with the VLA and VLBA, respectively. Using a 3σ channel sensitivity of ≈48 mJy from our VLA observations (see Table 1), a velocity spread of the masers of three channels, and $d = 436$ pc, Equation (2) gives an H_2O luminosity of $6 \times 10^{-11}\,L_{\odot}$. Assuming the correlation between $L_{\rm H_2O}$ and $L_{\rm Bol}$ found by Shirley et al. (2007) for high-luminosity YSOs, according to which

$$L_{\rm H_2O} = 3 \times 10^{-9} L_{\rm Bol}^{0.94}, \quad (3)$$

this upper limit in H_2O luminosity corresponds to $L_{\rm Bol} \approx 0.02\,L_{\odot}$. Thus, our VLA observations were in principle sensitive enough to

detect all H_2O masers associated to low-luminosity protostars in Serpens South with $L_{Bol} \gtrsim 0.02\,L_{\odot}$. As noted by Gómez et al. (2017), the correlation between bolometric and maser luminosities may not hold for the lowest-luminosity YSOs. We plot in the right panel of Figure 9 the bolometric luminosities of the four objects that have water masers and the maser luminosities measured at each individual epoch observed with the VLA and the VLBA. Due to the strong variability in both flux and velocity spread of the maser emission, the L_{H_2O} changes in all sources by more than one order of magnitude. CARMA-6 shows the highest variability, since the nondetection with the VLA implies a change in L_{H_2O} by about four orders of magnitude. In Figure 9, the two stars detected with the VLBA (SSTgbs J1830177–021211 and CARMA-6) fall, within one order of magnitude, close to their predicted position by the L_{H_2O} versus L_{Bol} empirical relationship. A scatter of one order of magnitude was also observed for this relationship (Shirley et al. 2007; their Figure 3).

5. Conclusions

We have conducted an interferometric survey of 22 GHz H_2O masers toward the low-mass star-forming region Serpens South. Our observations were first carried out with the VLA covering all known protostars (Class 0–Class I objects) across the region. The VLA observations revealed, for the first time, three water masers in the region, which are found to be associated to CARMA-7, SSTgbs J1830177–021211, and SSTgbs J1829053–014156. Follow-up VLBA observations were carried out toward the VLA-detected sources to investigate the spatial distribution and kinematics of the masers. The VLBA observations found water maser emission associated to CARMA-6, which had not been detected with the VLA.

Three water maser sources (CARMA-7, SSTgbs J1829053–014156, and CARMA-6) are associated with Class 0–Class I objects that drive large-scale molecular outflows and also display radio continuum emission from ionized gas. The water masers are found at the base of the molecular outflows and we propose that in all these three objects the masers are excited in shocks driven by the interaction between a protostellar jet and the circumstellar material. On the other hand, the source responsible for the excitation of the water maser associated with SSTgbs J1830177–021211 is unknown. This source has been classified in the literature as a Class II object and has no associated molecular outflows or radio jets. The small relative proper motions of two maser features that persisted over two epochs and the small parallax hinted by the astrometric fits to the brightest feature suggest that SSTgbs J1830177–021211 is most likely a background AGB star with the water masers tracing an expanding or contracting circumstellar envelope. Further VLBI observations will allow us to obtain the parallax and proper motions of the maser spots, to test the proposed mechanism for the water maser excitation in these objects, and confirm the AGB scenario proposed for SSTgbs J1830177–021211.

We also investigate the distributions of the bolometric luminosity of sources hosting 22 GHz H_2O masers and 162 YSOs covered by our observations. The comparison of the two distributions suggest a luminosity threshold for the water maser emission of $L_{Bol} \approx 10\,L_{\odot}$. However, the water masers show strong variability, thus lower-luminosity sources may have been missed by the observations.

Lastly, we detected 11 new sources with radio continuum emission at 22 GHz, of which six are known or candidate YSOs and five are unknown sources without counterparts at any other wavelength. Based on the estimation of the number of expected background sources in the observed area, we suggest that all of these unclassified sources are probably extragalactic objects.

The authors are grateful to the anonymous referee, whose comments helped to improve this paper. G.N.O.-L. acknowledges support from the von Humboldt Stiftung. L.L. acknowledges the support of DGAPA/PAPIIT grants IN112417 and IN112820, CONACyT-AEM grant 275201, and CONACyT-CF grant 263356. The authors acknowledge MiaoMiao Zhang for sharing the Canada–France–Hawaii Telescope near-infrared data. The National Radio Astronomy Observatory is a facility of the National Science Foundation operated under a cooperative agreement by Associated Universities, Inc. This paper makes use of the following ALMA data: ADS/JAO. ALMA #2012.1.00769.S and #2015.1.00283.S.

Appendix
Supplementary Figures

In this Appendix, we show maps of radio continuum emission from the VLA data toward water maser sources (Figure 10), YSOs with no detected water masers (Figure 11), and candidate extragalactic sources (Figure 12).

Figure 13 displays a 347 GHz ALMA continuum map of CARMA-6.

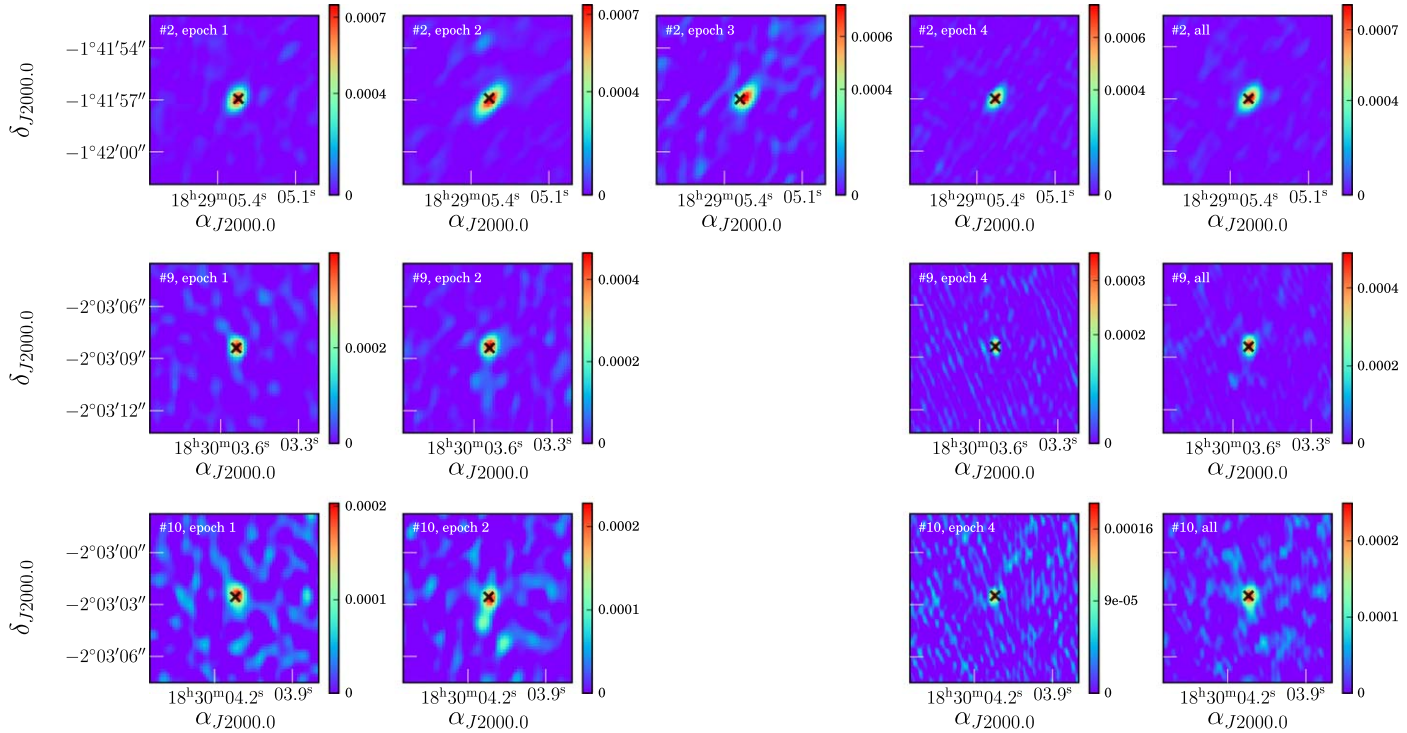

Figure 10. Maps of radio continuum emission obtained with the VLA. The first four columns correspond to epochs 1, 2, 3, and 4, respectively (see Table 1). The last column shows the maps of the combination of epochs 1, 2, and 4. The color scale is in Jy beam^{-1}. Shown are YSOs with detected water masers, whose mean positions are indicated by the black crosses.

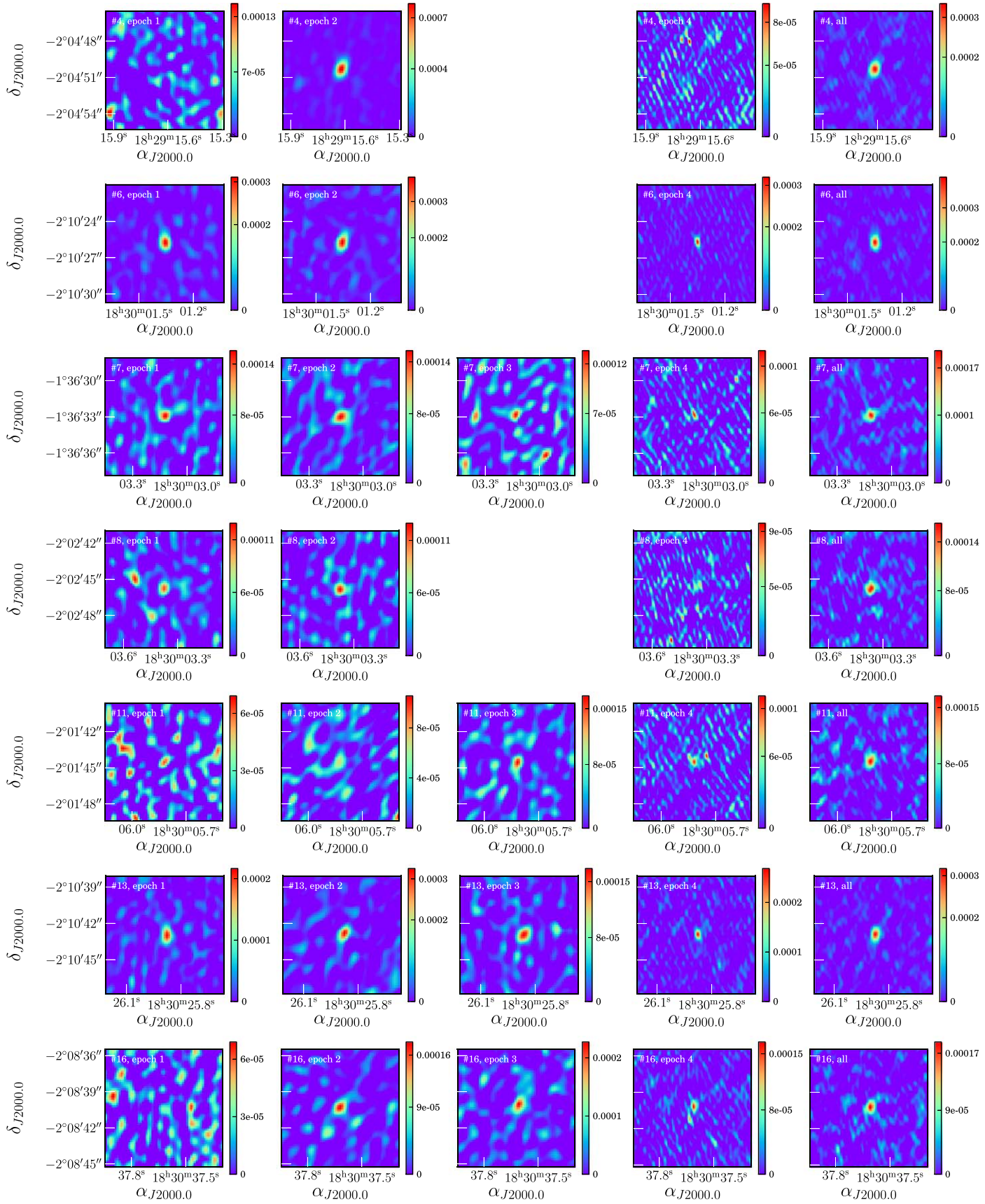

Figure 11. As Figure 10 for known or candidate YSOs and no detected water masers.

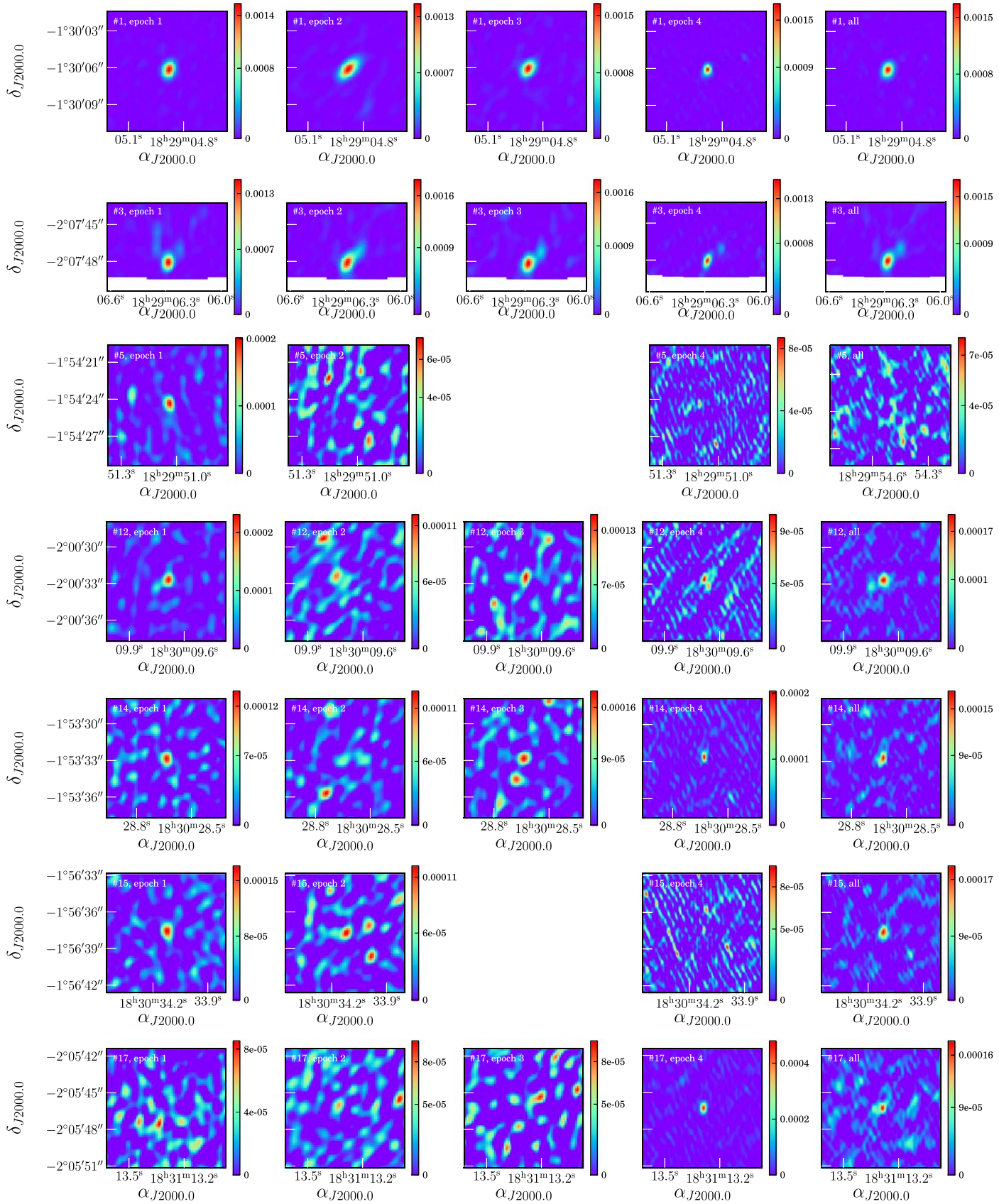

Figure 12. As Figure 10 for candidate extragalactic sources.

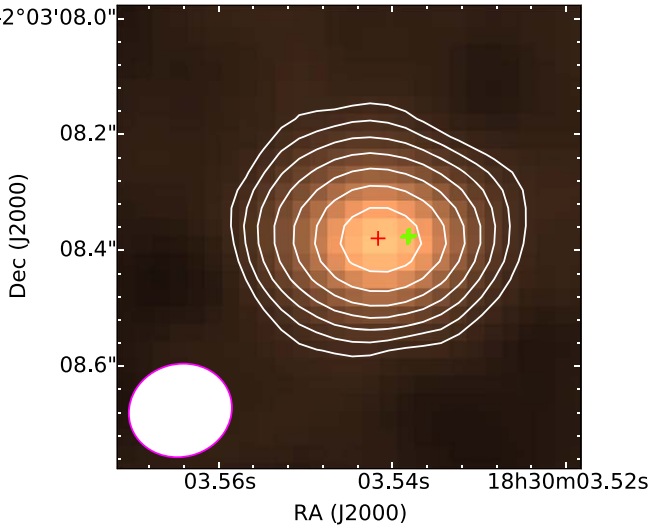

Figure 13. ALMA continuum emission at 347 GHz from CARMA-6 (color scale and white contours). The nth contour is at $(\sqrt{2})^n \times S_{\max} \times p$, where $S_{\max} = 0.074$ Jy beam^{-1}, $n = 0, 1, 2, 3, 4$ ..., and $p = 10\%$. The green crosses indicate the positions of the water masers and the red cross correspond to the position of the ALMA continuum peak. The sizes of the crosses indicate three times the astrometric accuracy of ALMA (9 mas) at 347 GHz. The beam size is shown in white in the bottom left corner.

ORCID iDs

Gisela N. Ortiz-León https://orcid.org/0000-0002-2863-676X
Adele L. Plunkett https://orcid.org/0000-0002-9912-5705
Laurent Loinard https://orcid.org/0000-0002-5635-3345
Sergio A. Dzib https://orcid.org/0000-0001-6010-6200
Carolina B. Rodríguez-Garza https://orcid.org/0000-0001-8286-2795
Thushara Pillai https://orcid.org/0000-0003-2133-4862
Yan Gong https://orcid.org/0000-0002-3866-414X
Andreas Brunthaler https://orcid.org/0000-0003-4468-761X

References

André, P., Men'shchikov, A., Bontemps, S., et al. 2010, A&A, 518, L102
Andre, P., Ward-Thompson, D., & Barsony, M. 1993, ApJ, 406, 122
Anglada, G., Villuendas, E., Estalella, R., et al. 1998, AJ, 116, 2953
Chen, X., Arce, H. G., Zhang, Q., Launhardt, R., & Henning, T. 2016, ApJ, 824, 72
Cheung, A. C., Rank, D. M., Townes, C. H., Thornton, D. D., & Welch, W. J. 1969, Natur, 221, 626
Claussen, M. J., Marvel, K. B., Wootten, A., & Wilking, B. A. 1998, ApJL, 507, L79
Claussen, M. J., Wilking, B. A., Benson, P. J., et al. 1996, ApJS, 106, 111
Condon, J. J., Cotton, W. D., Greisen, E. W., et al. 1998, AJ, 115, 1693
Davis, C. J., Gell, R., Khanzadyan, T., Smith, M. D., & Jenness, T. 2010, A&A, 511, A24
Dunham, M. M., Allen, L. E., Evans, N. J., II, et al. 2015, ApJS, 220, 11
Dzib, S. A., Ortiz-León, G. N., Hernández-Gómez, A., et al. 2018, A&A, 614, A20
Eiroa, C., Djupvik, A. A., & Casali, M. M. 2008, in Handbook of Star Forming Regions (The Southern Sky Vol. 2) ed. B. Reipurth (San Francisco, CA: ASP), 693
Fiebig, D., Duschl, W. J., Menten, K. M., & Tscharnuter, W. M. 1996, A&A, 310, 199
Furuya, R. S., Kitamura, Y., Saito, M., Kawabe, R., & Wootten, H. A. 1999, ApJ, 525, 821
Furuya, R. S., Kitamura, Y., & Shinnaga, H. 2008, PASJ, 60, 421
Furuya, R. S., Kitamura, Y., Wootten, A., Claussen, M. J., & Kawabe, R. 2003, ApJS, 144, 71
Furuya, R. S., Kitamura, Y., Wootten, H. A., et al. 2000, ApJL, 542, L135
Furuya, R. S., Kitamura, Y., Wootten, H. A., Claussen, M. J., & Kawabe, R. 2001, ApJL, 559, L143
Gaia Collaboration, Brown, A. G. A., Vallenari, A., et al. 2021, A&A, 650, C3
Gaia Collaboration, Prusti, T., de Bruijne, J. H. J., et al. 2016, A&A, 595, A1
Gómez, J. F., Palau, A., Uscanga, L., Manjarrez, G., & Barrado, D. 2017, AJ, 153, 221
Greisen, E. W. 2003, ASSL, 285, 109
Gutermuth, R. A., Bourke, T. L., Allen, L. E., et al. 2008, ApJL, 673, L151
Herczeg, G. J., Kuhn, M. A., Zhou, X., et al. 2019, ApJ, 878, 111
Hirota, T., Tsuboi, M., Kurono, Y., et al. 2014, PASJ, 66, 106
Hollenbach, D., Elitzur, M., & McKee, C. F. 2013, ApJ, 773, 70
Imai, H., Nakashima, K., Bushimata, T., et al. 2007, PASJ, 59, 1107
Kern, N. S., Keown, J. A., Tobin, J. J., Mead, A., & Gutermuth, R. A. 2016, AJ, 151, 42
Kettenis, M., van Langevelde, H. J., Reynolds, C., & Cotton, B. 2006, in ASP Conf. Ser. 351, Astronomical Data Analysis Software and Systems XV, ed. C. Gabriel et al. (San Francisco, CA: ASP), 497
Kirk, H., Myers, P. C., Bourke, T. L., et al. 2013, ApJ, 766, 115
Könyves, V., André, P., Men'shchikov, A., et al. 2015, A&A, 584, A91
Kounkel, M., Hartmann, L., Loinard, L., et al. 2017, ApJ, 834, 142
Lada, C. J. 1987, in IAU Symp. 115, Star Forming Regions, ed. M. Peimbert & J. Jugaku (Cambridge: Cambridge Univ. Press), 1
Lee, C.-F., Ho, P. T. P., Li, Z.-Y., et al. 2017, NatAs, 1, 0152
Maury, A. J., André, P., Men'shchikov, A., Könyves, V., & Bontemps, S. 2011, A&A, 535, A77
Maury, A. J., André, P., Testi, L., et al. 2019, A&A, 621, A76
Moscadelli, L., Li, J. J., Cesaroni, R., et al. 2013, A&A, 549, A122
Moscadelli, L., Sanna, A., Goddi, C., et al. 2019, A&A, 631, A74
Moscadelli, L., Sanna, A., Goddi, C., et al. 2020, A&A, 635, A118
Moscadelli, L., Testi, L., Furuya, R. S., et al. 2006, A&A, 446, 985
Nakamura, F., Ishii, S., Dobashi, K., et al. 2019, PASJ, 71, S3
Nakamura, F., Sugitani, K., Shimajiri, Y., et al. 2011, ApJ, 737, 56
Oliveira, I., Merín, B., Pontoppidan, K. M., et al. 2009, ApJ, 691, 672
Ortiz-León, G. N., Dzib, S. A., Kounkel, M. A., et al. 2017, ApJ, 834, 143
Ortiz-León, G. N., Loinard, L., Dzib, S. A., et al. 2018, ApJL, 869, L33
Ortiz-León, G. N., Loinard, L., Mioduszewski, A. J., et al. 2015, ApJ, 805, 9
Plunkett, A. L., Arce, H. G., Corder, S. A., et al. 2015a, ApJ, 803, 22
Plunkett, A. L., Arce, H. G., Mardones, D., et al. 2015b, Natur, 527, 70
Plunkett, A. L., Fernández-López, M., Arce, H. G., et al. 2018, A&A, 615, A9
Podio, L., Tabone, B., Codella, C., et al. 2021, A&A, 648, 45
Povich, M. S., Kuhn, M. A., Getman, K. V., et al. 2013, ApJS, 209, 31
Reid, M. J., Menten, K. M., Brunthaler, A., et al. 2009, ApJ, 693, 397
Sanna, A., Reid, M. J., Dame, T. M., Menten, K. M., & Brunthaler, A. 2017, Sci, 358, 227
Shirley, Y. L., Claussen, M. J., Bourke, T. L., Young, C. H., & Blake, G. A. 2007, ApJ, 667, 329
Thompson, A. R., Moran, J. M., & Swenson, G. W., Jr. 2017, Interferometry and Synthesis in Radio Astronomy (3rd ed.; Berlin: Springer)
Torrelles, J. M., Gómez, J. F., Rodríguez, L. F., et al. 1998, ApJ, 505, 756
Volvach, L. N., Volvach, A. E., Larionov, M. G., et al. 2019, A&A, 628, A89
Wilking, B. A., Claussen, M. J., Benson, P. J., et al. 1994, ApJL, 431, L119
Winston, E., Wolk, S. J., Gutermuth, R., & Bourke, T. L. 2018, AJ, 155, 241
Wu, Y. W., Sato, M., Reid, M. J., et al. 2014, A&A, 566, A17
Zhang, M., Fang, M., Wang, H., et al. 2015, ApJS, 219, 21
Zucker, C., Speagle, J. S., Schlafly, E. F., et al. 2019, ApJ, 879, 125